High-speed DNA-based rolling motors powered by RNase H

Kevin Yehl[1], Andrew Mugler[2,3], Skanda Vivek[2], Yang Liu[1], Yun Zhang[1], Mengzhen Fan[1], Eric R. Weeks[2] and Khalid Salaita[1]*

DNA-based machines that walk by converting chemical energy into controlled motion could be of use in applications such as next-generation sensors, drug-delivery platforms and biological computing. Despite their exquisite programmability, DNA-based walkers are challenging to work with because of their low fidelity and slow rates (~1 nm min⁻¹). Here we report DNA-based machines that roll rather than walk, and consequently have a maximum speed and processivity that is three orders of magnitude greater than the maximum for conventional DNA motors. The motors are made from DNA-coated spherical particles that hybridize to a surface modified with complementary RNA; the motion is achieved through the addition of RNase H, which selectively hydrolyses the hybridized RNA. The spherical motors can move in a self-avoiding manner, and anisotropic particles, such as dimerized or rod-shaped particles, can travel linearly without a track or external force. We also show that the motors can be used to detect single nucleotide polymorphism by measuring particle displacement using a smartphone camera.

Inspired by biological motors, a number of synthetic motors have been developed as model systems that employ a wide range of chemical reactions[1–6]. DNA-based machines that walk along a track have shown the greatest promise in recapitulating the properties of biological motor proteins[1,7–14]. However, the maximum distance travelled by the most-processive DNA-based motors is 1 μm (refs 8,9,12). The velocity of these walkers is also limited to rates of ~1 nm min⁻¹ because of a fundamental trade-off between motor endurance and speed. The problem is that DNA walkers tend to dissociate off their tracks spontaneously and, although increasing the motor multivalency improves the track affinity and motor endurance (the mean distance travelled), this leads to a significant decrease in motor velocity. For example, increasing the multivalency of a DNAzyme-based motor from two anchors to six led to complete abrogation of the motor transport[15].

Yet, for DNA-based machines to transition beyond an elegant model system for motor proteins and truly achieve their potential, both motor efficiency and velocity need to be enhanced by orders of magnitude. In addition, the sophisticated instrumentation currently required to observe DNA walkers needs to be simplified greatly to render DNA machines as useful. To overcome these challenges, we designed a highly multivalent motor that moves through a cog-and-wheel mechanism, which allows micrometre- or nanometre-sized particles to roll rather than walk. Rolling represents a fundamentally distinct type of movement that overcomes the documented trade-offs inherent to multivalent molecular motors[15,16]. In principle, this is because rolling reduces the DNA motor footprint, which reduces unproductive sampling interactions and thus increases the velocity.

Design and synthesis of spherical motors powered by RNase H

The motor consists of a DNA-coated spherical particle (5 μm or 0.5 μm diameter) that hybridizes to a surface modified with complementary RNA. The particle moves upon the addition of RNase H, which selectively hydrolyses hybridized RNA but not single-stranded RNA (ssRNA) (Fig. 1). As the driving force for movement

is derived from the free energy of binding new ssRNA that biases Brownian motion away from consumed substrate (Fig. 1a), this type of motion is often described as a 'burnt-bridge Brownian ratchet'. The molecular walkers also employ a burnt-bridge mechanism, in which oligonucleotide hybridization is followed by DNAzyme/endonuclease hydrolysis of the fuel strand. The main difference between the molecular walkers and our system is the massive multivalency of the DNA-coated particles; molecular walkers typically employ 2–6 anchor points whereas our particle-based motor employs thousands of anchoring strands. This equates to a 100–1,000-fold greater contact area or a 10–40-fold greater contact diameter with the surface when compared with that of molecular spiders. This micrometre-sized length of the particle significantly increases the number of contacts with the surface, which should lead to collective and emergent properties not expected for DNA-based walkers. Importantly, we expected that our particles would overcome the diminished velocities caused by a high multivalency, as is predicted by theory, because the RNase H hydrolysis rate is approximately two orders of magnitude greater than that of DNAzymes and endonucleases[14,17,18]. Moreover, highly multivalent motors are expected to display greater processivity, and thus potentially address a major limitation of DNA walkers. Finally, the spherical particle template allows for the potential to roll, which is a fundamentally different mode for translocation of DNA-based machines.

We first generated an RNA monolayer on a substrate by immobilizing a DNA anchor strand to a thin gold film and then hybridizing a fluorescently labelled RNA–DNA chimera strand to the surface. A Cy3 fluorophore at the 3′ RNA terminus was used to optimize the RNA density and to detect RNA hydrolysis using fluorescence microscopy (Figs 1b and 2a,b, and Supplementary Fig. 1). With the optimized conditions, we achieved a maximum RNA density of 50,000 molecules μm⁻², equivalent to an average molecular footprint of 20 ± 6 nm² per RNA strand (Supplementary Fig. 2). This RNA density was maintained for at least four hours in 1× PBS (phosphate-buffered saline) and 10 μM dithiothreitol (DTT), a thiol-reducing agent necessary to maintain RNase H activity

[1]Department of Chemistry, Emory University, 1515 Dickey Drive, Atlanta, Georgia 30322, USA. [2]Department of Physics, Emory University, 400 Dowman Drive, Atlanta, Georgia 30322, USA. [3]Department of Physics, Purdue University, West Lafayette, Indiana 47907, USA. *e-mail: k.salaita@emory.edu
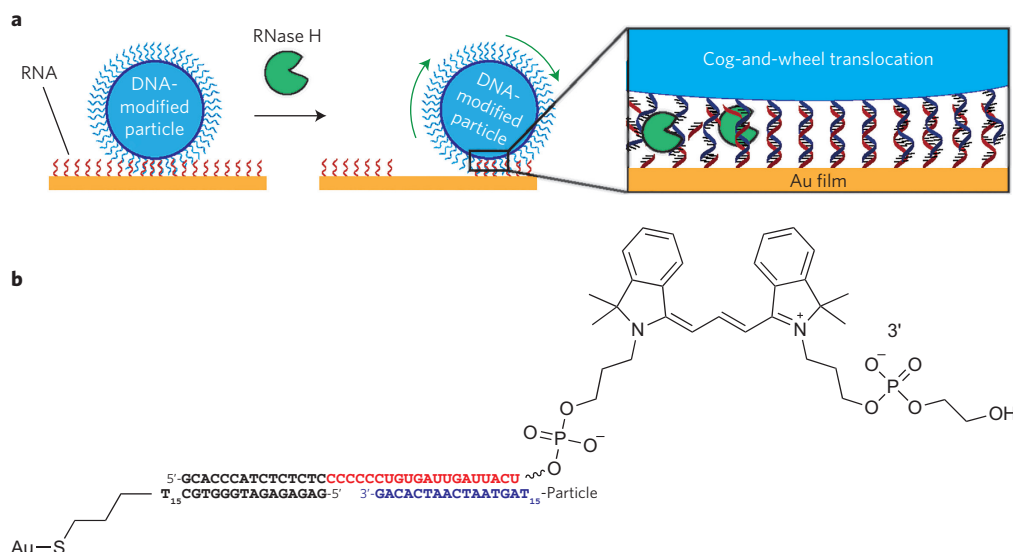
Figure 1 | Approach used to generate RNA-fuelled, enzyme-catalysed autonomous DNA motors. a, DNA-modified particles were hybridized to an RNA monolayer that presented a complementary strand. Particles were immobile until RNase H was added, which selectively hydrolyses RNA duplexed to DNA. **b**, The schematic representation shows the hybridized oligonucleotide sequences at the particle–substrate junction (there are hundreds of duplexes within this junction). RNA bases are shown in red and the particle DNA bases are shown in blue.

(Supplementary Fig. 3). In the absence of DTT, the surfaces were stable for weeks in 1 × PBS.

Given that particle motion is connected intimately with RNase H efficiency and enzyme rates vary when substrates are immobilized, we initially measured the hydrolysis kinetics for a DNA–RNA duplex monolayer. We found that polyethylene glycol (PEG) passivation was critical, because RNase H was inhibited when the surface was incompletely passivated (Supplementary Fig. 4)[19,20]. For optimally passivated surfaces, we measured the turnover number (k_{cat}) for RNA hydrolysis catalysed by RNase H to be $k_{cat} = 25$ min^{-1}. This rate is 6,000-fold greater than the turnover number for nanoparticle-immobilized DNAzymes, which thus supports our expectation that rolling motors powered by RNase H may achieve rapid velocities (Supplementary Fig. 5)[17,18].

DNA-functionalized particles with a density of ~91,000 molecules μm^{-2} (footprint of 11 ± 3 nm^2 per DNA strand) (Supplementary Fig. 6) were then synthesized and hybridized to a substrate that presented the complementary RNA strand. Importantly, the DNA density matched that of the RNA density on the planar substrate to ensure a high degree of polyvalency (~10^4 contacts μm^{-2}) and therefore minimize motor detachment from the substrate and maximize run processivity. The particles remained immobile until RNase H was added, which led to a rapid translocation of the particles across the substrate. This was tracked quantitatively by finding the centroid of the particles in time-lapse brightfield (BF) microscopy at five second intervals (Fig. 2c, Supplementary Fig. 7 and Supplementary Movie 1)[21]. Importantly, the BF-generated tracks matched the wide-field fluorescence depletion tracks (full-width at half-maximum (FWHM) of 720 ± 110 nm), which confirms that the particle motion was associated with continuous RNA hydrolysis (Fig. 2c,d, Supplementary Fig. 8 and Supplementary Movies 2 and 3). The line-scan analysis of the fluorescence depletion indicates that ~50% of the RNA underneath the particle is hydrolysed (Fig. 2d). Structured illumination microscopy (SIM), a super-resolution microscopy technique with ~110 nm resolution, revealed a more-accurate footprint of the particle–substrate junction that corresponded to an average track width of 380 ± 50 nm (n = 55 tracks) (Fig. 2e and Supplementary Fig. 9). This footprint indicates a maximum of ~5,500 DNA–RNA surface contacts at the motor–substrate junction (Supplementary Fig. 10). Importantly, substrates comprised of DNA

did not lead to any translocation on the addition of RNase H (Supplementary Fig. 7), which confirms that the particle motion is specific to RNA hydrolysis at the particle–substrate junction.

Motors travel in a self-avoiding fashion

In principle, the particle motion should be biased away from the consumed RNA substrate and towards new regions that had not been sampled previously. To investigate this model, the particle motion was analysed by plotting the mean squared displacement (MSD) against time t, because MSD is known to be proportional to t^α for scaling exponent α (ref. 22). However, we found that the MSD versus time did not have a linear dependence, as is the case for random diffusion ($\alpha = 1$), but rather a power dependence with $\alpha = 1.45 \pm 0.20$, which indicates that particle motion is not well described by random diffusion (Fig. 2f) (a histogram that summarizes the distribution of diffusional exponents is given in Supplementary Fig. 11). Moreover, random diffusion is known to have displacement distributions in the form of $P(x) \propto \exp(-A|x|^\nu)$ for prefactor A and exponent $\nu = 2$, yet we measured $\nu = 4.3 \pm 1$ (Supplementary Fig. 12). This, again, further supports that the motion is biased away from hydrolysed substrate.

We then asked whether particle motion can be described by a self-avoiding random walk, in which a particle cannot cross its own path but otherwise moves randomly. To the best of our knowledge, these types of self-avoiding random walks have only been theoretical, and not realized experimentally. As self-avoiding diffusion is typically studied using polymer chains[23], we conducted a multivalent stochastic simulation of hundreds of particles to predict the values for α and ν associated with self-avoiding random diffusion (Supplementary Discussion 1 and Supplementary Movie 4). This modelling revealed that over short distances (short timescales) the particles exhibit tethered diffusion (MSD $\propto t^\alpha$, with $\alpha = 1$), and over long distances the particles exhibit the scaling MSD $\propto t \log(t)$, which is theoretically expected for self-avoiding behaviour (Supplementary Discussion 1)[24,25]. The rate of data acquisition falls in the transition region between these two timescales, in which simulations predict a power-law MSD scaling with $\alpha = 1.49 \pm 0.05$ and a displacement distribution with $\nu = 3.8 \pm 0.1$, both in agreement with the measured values (Supplementary Discussion 1). These findings demonstrate that DNA-powered particle motors execute motion that is statistically
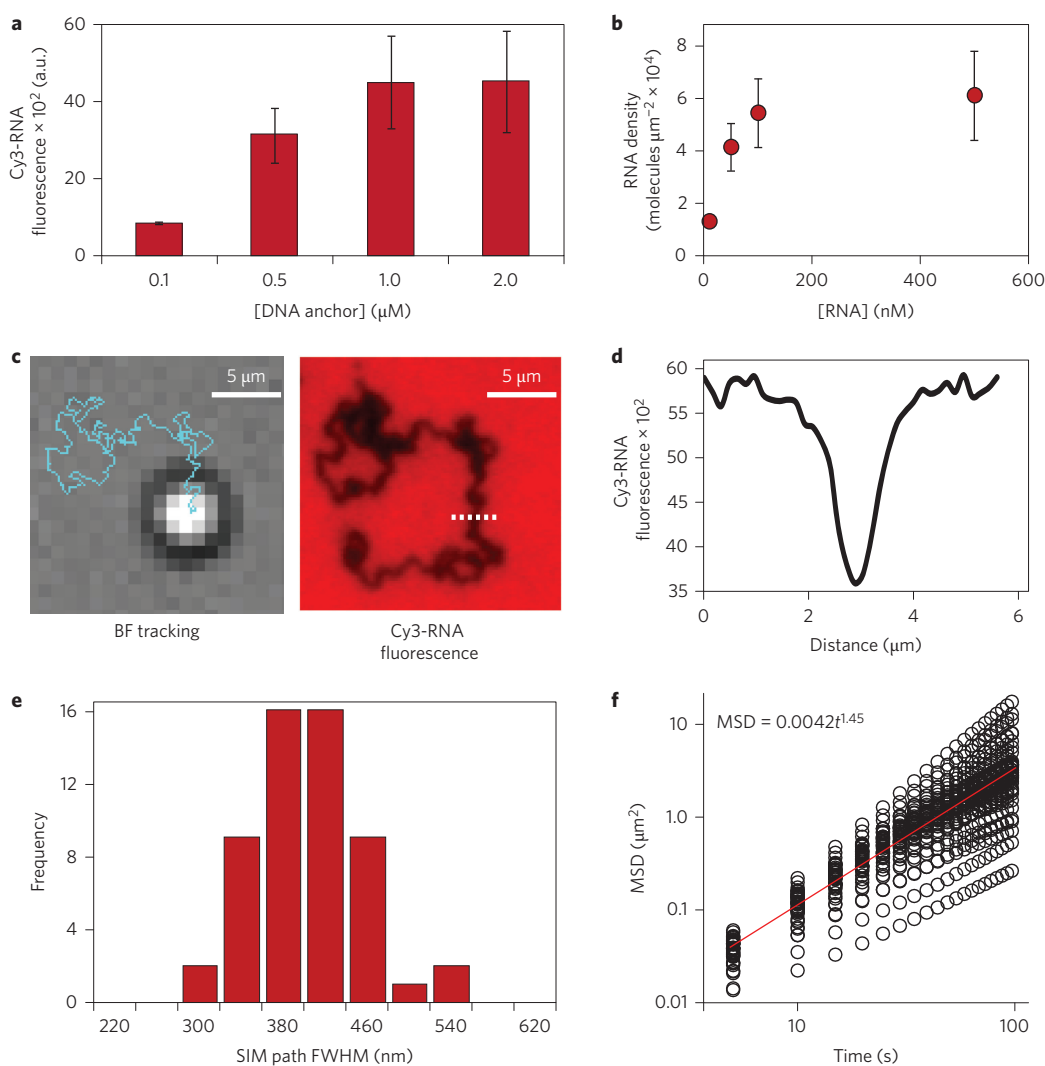
Figure 2 | Characterization of particle motion driven by RNase H. a, The bar graph shows how the incubation concentration of the DNA anchor strand alters the Cy3-RNA fluorescence intensity, which is directly proportional to the RNA surface density. The maximum RNA surface density was achieved when the incubation concentration of the DNA anchor strand was equal to or greater than 1 μM. Error bars represent the s.d. in the average fluorescence intensity from at least five regions across each channel. **b**, Plot of the RNA surface density as a function of RNA concentration during Cy3-RNA hybridization with the surface-immobilized DNA anchor strand. The RNA density was maximized when RNA was hybridized at a concentration of at least 100 nM. Error bars represent the s.d. in the average fluorescence intensity from at least five regions across each channel. **c**, Representative BF image and trajectory (blue line) from a time-lapse movie that tracked a single microparticle 30 minutes after the RNase H addition. The same region was then imaged in the Cy3 fluorescence channel to reveal the location of depleted Cy3 signal. **d**, The line-scan plot of the dotted white line in **c** shows the depletion track from the wide-field fluorescence image. **e**, Histogram analysis of the FWHM of the depletion-path width acquired using SIM. **f**, Log(MSD) versus time analysis from individual particle trajectories (*n* = 43), which is shown with black circles and plotted on a logarithmic scale. The red line indicates the average slope derived from all the individual particle trajectories.

consistent with self-avoiding behaviour. To the best of our knowledge, rolling DNA-based motors provide the first experimental realization of the 'true' self-avoiding walker statistical process[24,26].

Mechanism of motor translocation
Particle motion could occur through three plausible mechanisms: (1) walking/sliding, (2) hopping and (3) rolling (Supplementary Fig. 13). The hopping mechanism was immediately ruled out on examination of the continuous fluorescence-depletion tracks (Fig. 2c). To differentiate between the two remaining mechanisms, particles were hybridized to an RNA substrate, and the unbound DNA on the particle was blocked by hybridization with a complementary DNA strand (Fig. 3a). If motion primarily occurs through a walking/sliding mechanism, we expected that the particles would move in a processive fashion to leave behind an RNA depletion track. However, on RNase H addition the particles

diffused randomly to produce $\alpha = 0.99 \pm 0.22$ and $v = 1.8 \pm 0.8$, and no corresponding RNA depletion tracks were observed (Fig. 3b,c, Supplementary Discussion 1, Supplementary Fig. 11 and Supplementary Movie 5). As the hopping and walking/sliding mechanisms of motion are ruled out, we conclude that the particles primarily translocate by rolling in a monowheel or in a cog-and-wheel fashion. The rolling mechanism of motion was further confirmed through two other sets of experiments (*vide infra*). This is the first example of a DNA-based autonomous rolling motor, and we subsequently refer to these machines as monowheels.

For the particles to move in a cog-and-wheel mechanism, the following sequence of reactions must occur: (1) RNA hydrolysis, (2) DNA unbinding (k_{off}) from the hydrolysed substrate, (3) tethered particle diffusion (rolling) and (4) DNA hybridization to new RNA substrate (k_{on}) (Supplementary Fig. 14). To help determine the parameters that affect the particle velocity, we measured particle
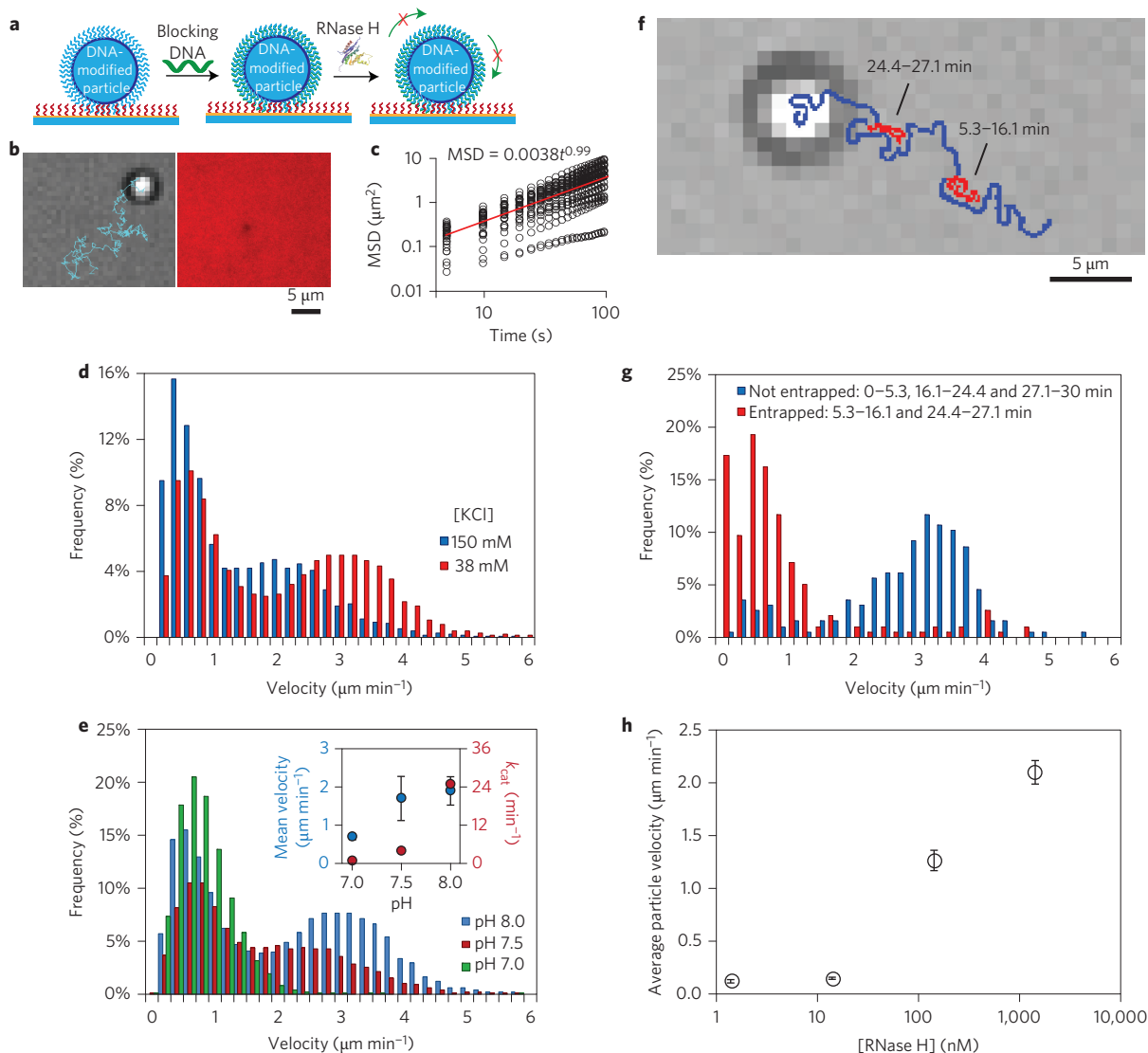
Figure 3 | Elucidating the mechanism of particle motion and determining factors that influence particle velocity. a, The schematic shows the strategy used to test whether particles roll during translocation by blocking the free DNA of the particle by hybridizing with a blocking DNA strand (green). **b**, Representative BF image and trajectory (blue) taken from a time-lapse movie tracking a single particle that had been blocked with DNA and treated with RNase H. The same region was imaged using the Cy3 fluorescence channel, which indicates the lack of a RNA hydrolysis track. It is typical for a small transient spot with a lower fluorescence intensity (see the centre of the fluorescence image) to be observed under particles and so this is not a result of RNA hydrolysis. **c**, Log(MSD) versus time plot of particle diffusion for the blocked particles, which is plotted on a logarithmic scale. The black circles represent individual data points from $n = 32$ particles and the red line indicates the average of these plots. **d**, Histogram analysis of particle velocity for each five second interval as a function of [KCl]; 38 mM (red, $n = 43$ particles (15,480 occurrences)) and 150 mM (blue, $n = 52$ particles (18,720 occurrences)). **e**, Histogram analysis of the particle velocity for each five second interval as a function of pH; 8.0 (blue, $n = 43$ particles (15,480 occurrences)), 7.5 (red, $n = 50$ particles (18,000 occurrences)) and 7.0 (green, $n = 26$ particles (9,360 occurrences)). The inset compares RNase H k_{cat} (red) and average particle velocity (blue) as a function of pH. **f**, Representative BF image and trajectory (blue and red) taken from a time-lapse movie that tracked a single particle for 30 minutes; the red section indicates when the particle becomes entrapped. **g**, Representative velocity histogram of an individual particle when the particle is entrapped (red) or not entrapped (blue). Entrapment leads to a significant decrease in particle velocity. **h**, Plot of the particle-velocity dependence on RNase H concentration. In the absence of RNase H, the particles do not move. Error bars represent the standard deviation from $n = 3$ experiments. Most experiments were performed with [RNase H] = 144 nM.

translocation as a function of monovalent and divalent salt concentrations, pH and RNase H concentration. Under a high salt concentration we expected that the rate of hybridization (k_{on}) would increase, whereas the rate of dehybridization (k_{off}) would decrease, and that under decreasing pH, k_{cat} would decrease. We found that the particle velocity is highly dependent on salt concentration and decreases under higher ionic strengths (Supplementary Movie 6). In contrast, the particle speed is only sensitive to k_{cat} when k_{cat} is below 0.4 min^{-1} (Fig. 3d,e, Supplementary Fig. 15 and Supplementary Movies 1, 7 and 8). Taken together, these results suggest that k_{off}

acts as the kinetic bottleneck for particle motion at pH 7.5 or greater (Supplementary Fig. 14).

Interestingly, the particle-speed histogram contains two populations (Fig. 3d). On further analysis of individual particle velocities and accounting for stage drift, the two populations correspond to two states for each particle, a slow/stalled state and a fast state, as opposed to two types of particles or contributions owing to stage drift (Supplementary Fig. 16). The slower state results from a transient stalling of the particle, which may be attributed to factors (including surface defects) that lead to nonspecific particle binding, inactive

enzyme bound to the particle-substrate junction and particle self-entrapment. On a detailed analysis of individual particle trajectories, we found that stalling mostly correlated to particle self-entrapment (Fig. 3f,g and Supplementary Movie 9). To determine whether the enzyme concentration used, [RNase H] = 140 nM, saturated the available substrate-binding sites, the monowheel velocity was monitored as a function of enzyme concentration (Fig. 3h and Supplementary Fig. 17). At a tenfold greater enzyme concentration, only a slight increase in average velocity was observed, whereas tenfold and 100-fold dilutions of RNase H led to near abolition of the monowheel motion. The particle-speed histograms for decreasing RNase H concentration (Supplementary Fig. 17) show a gradual decrease in velocity as opposed to a shift to the low-velocity population, which thus confirms that multiple RNase H enzymes are operating in parallel.

A general design rule for creating processive DNA machines necessitates that the rate of cleaving contacts and leg disassociation from the track is slower than the rate of forming new track contacts. The stochastic nature of association and disassociation rates implies that molecular DNA walkers occasionally disassociate from the track. This is reflected in the relatively low fidelity of molecular walkers[1,7–11]. A higher multivalency buffers against such spontaneous disassociation, and thus increases the run processivity[15,16,27]. Our analysis suggests that the monowheels are highly multivalent with at least ~1,000 DNA–RNA duplex contacts present at any given time. This estimate is based on the RNA depletion-track analysis, which indicates that 50% of RNA is hydrolysed within the ~400 nm wide track. Given the RNase H turnover rate of 25 min^{-1} and the RNA surface density (1×10^4 RNA μm^{-2}), the monowheels must have at least ~1,000 RNA–DNA duplexes occupied by RNase H to maintain a velocity of 2 μm min^{-1}. Fewer contacts would result in lower particle speeds. This is a lower-bound estimate of the particle multivalency because this calculation assumes that every duplex is bound by active enzyme, which is unlikely. Therefore, monowheels display a multivalency 2–3 orders of magnitude greater than that of molecular walkers, which affords significant improvement in motor processivity.

Another important difference between molecular walkers and our monowheels is the effect of gravity on micrometre-sized particles. Albeit small, the force of gravity (~0.6 pN for a 5 μm silica particle in water) may bias the observed processivity by limiting particle–surface dissociation. To determine the role of gravity on particle motion, we inverted the sample geometry such that monowheels were upside down, and so operated against the force of gravity (Supplementary Fig. 18). Under identical conditions, 80% of the inverted monowheels displayed similar speeds and processivity (distance travelled before stalling) as those of the upright samples. At [KCl] = 38 mM, 20% of the particles detached on flipping the sample, whereas at [KCl] = 75 mM, none of the observed particles detached from the surface and the monowheels displayed slightly enhanced velocities to those observed at [KCl] = 38 mM (either when the sample was upright or flipped). Therefore, the primary contributor to monowheel processivity is the high multivalency of the system rather than the force of gravity.

To simplify the analysis and quantification, we used 5 μm diameter particles for the majority of experiments. However, the rolling mechanism of translocation can be recapitulated with 0.5 μm diameter particles (Supplementary Fig. 19 and Supplementary Movie 10). In principle, these smaller particles reduce the maximum number of DNA–RNA contacts by one of order of magnitude to the range of several hundred. Similar maximum velocities up to 5 μm min^{-1} and average velocities of 1.8 ± 0.4 and 1.9 ± 0.5 μm min^{-1} were observed for both 0.5 and 5 μm particles, respectively, which shows that the fundamental cog-and-wheel mechanism of rolling is independent of cargo size within the range tested (Supplementary Fig. 19). This was initially surprising because the smaller particles have fewer contacts with the surface and reduced drag, which results in a faster k_{off}, and thus were expected to

translocate more quickly. On further analysis, we found that the smaller particles are less multivalent, and therefore fewer RNA–DNA duplexes are available for hydrolysis at any given time. This is expected to slow down the absolute RNA hydrolysis rate and thus reduce the particle velocity. These opposing effects create a complex relationship between motor speed and particle size, and for the 5 μm beads compared with the 500 nm particles, the effect of particle size effectively cancels out, which leads to similar observed velocities. However, as expected, the less-multivalent 0.5 μm particles rolled for shorter average-run lengths compared with the 5 μm diameter particles (~3 μm versus ~200 μm), which continued to move processively throughout a 30 minute movie and even continued to move for over five hours (Supplementary Fig. 20). The decrease in run length for the 0.5 μm particles results from the lower multivalency (fewer contacts) with the surface, and thus increases the probability of detachment. Nonetheless, an increase in the KCl and Mg concentrations to 75 mM and 3 mM, respectively, enhances the 0.5 μm particle endurance such that the majority of particles display processive motion for the entire 30 minute movie (Supplementary Movie 11). This provides the 0.5 μm particles with an average run length of greater than 25 μm. Despite much work in the area of DNA-based machines, this class of multivalent rolling motor exceeds the velocity and processivity of previous DNA motors by three orders of magnitude and approaches the efficiency of biological enzymes, with velocities on the order of tens of micrometres per second and run lengths of hundreds of micrometres.

Track-guided unidirectional motion

To achieve unidirectional transport that resembles motor protein motion along a filament, RNA was spatially micropatterned into 3 μm wide tracks (Fig. 4a). Particles were then hybridized to the patterned RNA, and RNase H was added to initiate motion (Fig. 4b). Using BF time-lapse tracking and RNA fluorescence depletion, we observed that a subset of particles moved along the 3 μm substrate corral and unidirectionally deflected away from the PEG-printed regions (Supplementary Movie 12). Many particles became entrapped, partially because of RNA cross-contamination into the PEG-passivated regions (Fig. 4c) and partially because of self-entrapment in consumed substrate corrals. It is probable that generating well-passivated nanoscale RNA tracks commensurate in size with the width of particle–substrate junctions (~400 nm) will lead to an increased yield of linear trajectories[8]. Nonetheless, this provides a proof-of-concept demonstration of autonomous translocation using self-assembled components without an external field, akin to the motion of motor proteins.

Dimer and rod particles travel ballistically

An alternative strategy to achieve linear motion is to limit lateral particle motion by incorporating multiple monowheels on the body of a single chassis. This was investigated previously by Diehl *et al.*, but given the unique rolling mechanism for our system, we speculated that multiple motors could only result in ballistic or linear motion[27]. By happenstance, we found that a 1–10% subset of our particles were fused and so form dimers, a common by-product in silica-particle synthesis. We found that these particles travelled linearly for distances that spanned hundreds of micrometres at a velocity of ~0.6 ± 0.5 μm min^{-1}, $n = 68$ dimer particles (Fig. 4d and Supplementary Movies 13 and 14). Not surprisingly, a plot of MSD versus t for particle dimers showed a power-law scaling of $\alpha = 1.82 \pm 0.13$, which confirms that the particle motion was nearly linear ($\alpha = 2$). Also, we discovered that 50% of single spherical particles displayed a transient component of their trajectory that is linear and associated with wider tracks; linear motion was correlated with wider ~1.0 ± 0.1 μm tracks or multiple contact points (Supplementary Figs 8 and 9). The ballistic (linear) motion observed for what appears to be wider tracks may result from particles that
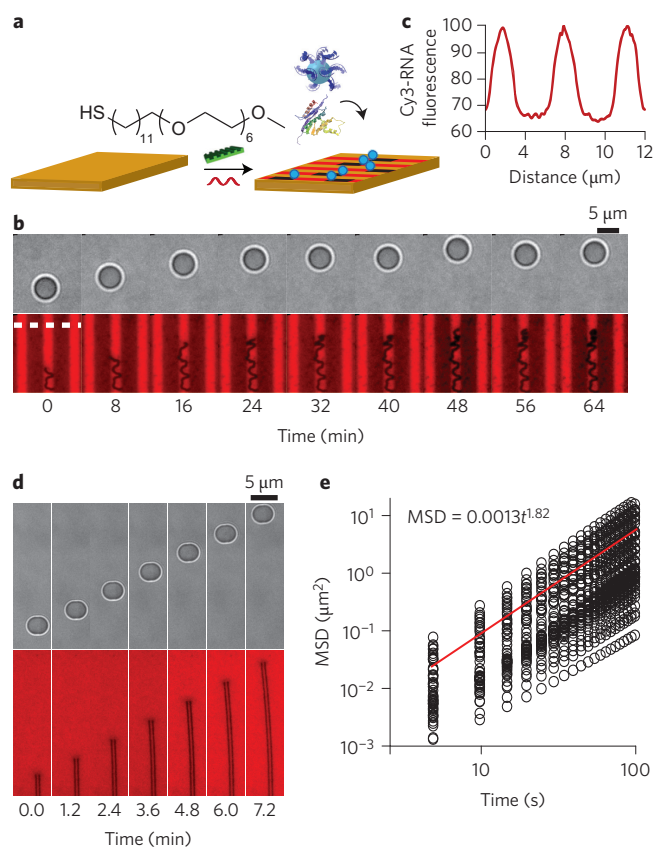
Figure 4 | Directional motor translocation from self-avoiding to ballistic.
a, The schematic shows the strategy used to generate RNA microtracks by microcontact printing. SH-PEG barriers were printed directly onto the gold film, which was backfilled with RNA. **b**, BF and fluorescence time-lapse images of a particle moving along a 3 μm wide track after the addition of RNase H. **c**, Line-scan analysis of the region highlighted in the fluorescence channel by a dotted white line in **b** shows the track dimensions and the effectiveness of the PEG barriers. **d**, Representative BF and fluorescence images taken from a time-lapse movie that tracked a dimerized particle after RNase H addition. The BF-analysed trajectory, as well as the two parallel fluorescence-depletion tracks, showed a near-linear particle motion. **e**, Log(MSD) versus time analysis of the dimerized particle motion which is plotted on a logarithmic scale. The slope of this plot shows an average power law dependence of 1.82 ± 0.13, which confirms that the particle dimer travelled in a ballistic linear fashion.

possess multiple contact points that cannot be resolved or from particles that roll along imperfections along the surface. After these observations, we synthesized DNA-coated microrods and anticipated a similar behaviour. The microrods showed a nearly linear motion, which demonstrates that the rolling mechanism is not limited to spherical particles (Supplementary Fig. 21). These are the first examples of directional motion without the need of a patterned track or external electromagnetic field, and is only afforded by the unique cog-and-wheel translocation mechanism.

Detection of single-nucleotide polymorphism (SNP)

As monowheel motion is exquisitely sensitive to k_{on}, k_{off} and k_{cat}, we anticipated that particle motion could provide a readout of molecular recognition. As a proof-of-concept, we aimed to detect a SNP mutation, which is a biomedically relevant and a challenging mutation to identify. Particles that display the SNP (5′-mAmGTAATTAAmUmC-3′) travelled ~60% slower (0.3 μm min^{-1}) than identical particles with a perfect match (5′-mAmGTAATCAAmUmC-3′) (Supplementary Fig. 22). This difference in velocity can be attributed to a slower rate of hydrolysis
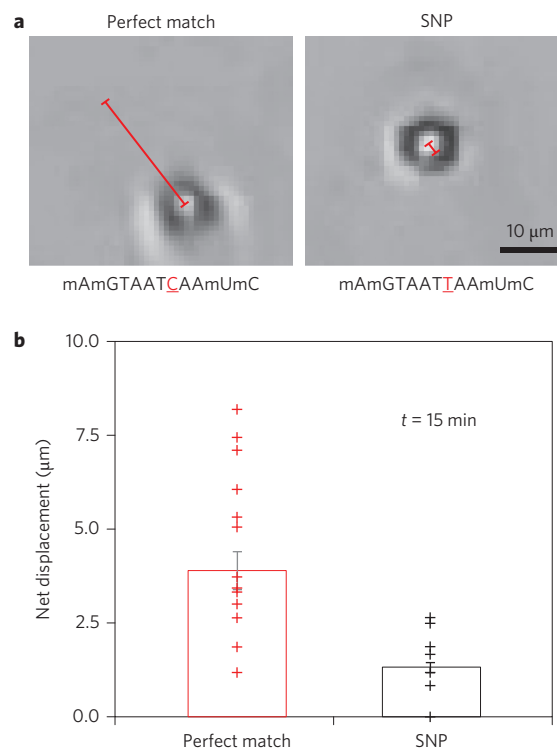
Figure 5 | SNP detection with a smartphone microscope. a, Representative BF images collected by using a smartphone microscope. The images show particles and their net displacement for a perfect match and the SNP sequences after RNase H addition ($t = 15$ min). The sequences are illustrated below each image in the 5′ to 3′ orientation with the single-base difference between sequences underlined and indicated in red and the non-natural 2′ methyl ether RNA modification indicated by the letter 'm' before the base (scale bar, 5 μm). Owing to the shorter recognition sequence, higher salt concentrations were used in the reaction buffer (75 mM Tris (pH = 8), 110 mM KCl and 4.5 mM MgCl$_2$). **b**, The scatter plot displays the particle net displacements 15 minutes after RNase H addition. The mean particle displacement is shown as the height of the bar. Error bars represent the s.d. from $n = 42$ particles total ($P < 0.0001$, as determined by a t-test with unequal variances).

for RNase H to hydrolyse duplexes that possess a single base mismatch[28]. Owing to the micrometre-sized cargo and large distances travelled, even a smartphone camera equipped with an inexpensive plastic lens can detect motion associated with this SNP by recording particle displacement within a short time interval ($t = 15$ min) (Fig. 5a,b). SNP detection could also be achieved using unmodified DNA (Supplementary Fig. 23), although a maximum discrimination required a shortened RNase H recognition sequence. Most importantly, the size and efficiency of the motors allow for a rapid and simple SNP sensing and represents a new application for DNA-based motors.

In conclusion, monowheels take advantage of multivalent substrate interactions to produce emergent collective properties that are difficult to predict a priori from the properties of the individual biomolecules[29–31]. Monowheels also achieve velocities up to ~5 μm min^{-1}, a speed that is ~5,000-fold greater than that of the fastest known synthetic DNA walker and approaches the velocities of biological motor proteins[8]. Monowheels use the same chemistry as molecular walkers—specific DNA–RNA hybridization followed by RNA hydrolysis. Moreover, the leg-to-leg spacing (DNA–DNA spacing) for the walkers is similar to the spacing between DNA strands for monowheels (~5 nm). However, the monowheels differ from the DNA walkers because of their massive multivalency, which leads to collective behaviours such as track-free linear motion

and rolling. Although highly multivalent motors typically display diminished speeds, monowheels break this trend because of the reduction in unproductive DNA–surface contacts enabled by rolling and the parallel activity of RNase H in a highly dense DNA–RNA contact (as suggested by modelling). Further experiments with anisotropic particles and different enzyme–substrate pairs will elucidate the role of these contributions. At best, the efficiency of converting chemical energy into mechanical work for monowheels is approximately 0.001%, which is on a par with chemically powered synthetic motors[32] and may be optimized further in the future (Supplementary Discussion 2). Owing to the multimicrometre-sized chassis and rapid translocation rates, real-time tracking of movement can be achieved with conventional optical microscopy and even a smartphone-based microscope, and thus circumvent the need for atomic force microscopy and analysis based on electron microscopy. As the cog-and-wheel rolling mechanism of motion is highly sensitive, monowheels represent an important step in bringing together the field of DNA-based sensing with the emerging area of DNA machines and motors. For example, motor velocity can probably be modulated by aptamer–analyte interactions, which suggests that monowheels will become a new and powerful tool in label-free sensing assays.

Methods

Methods and any associated references are available in the online version of the paper.

References

1. He, Y. & Liu, D. R. Autonomous multistep organic synthesis in a single isothermal solution mediated by a DNA walker. *Nature Nanotech.* **5**, 778–782 (2010).
2. Lewandowski, B. *et al.* Sequence-specific peptide synthesis by an artificial small-molecule machine. *Science* **339**, 189–193 (2013).
3. von Delius, M., Geertsema, E. M. & Leigh, D. A. A synthetic small molecule that can walk down a track. *Nature Chem.* **2**, 96–101 (2010).
4. Paxton, W. F., Sundararajan, S., Mallouk, T. E. & Sen, A. Chemical locomotion. *Angew. Chem. Int. Ed.* **45**, 5420–5429 (2006).
5. Pavlick, R. A., Sengupta, S., McFadden, T., Zhang, H. & Sen, A. A polymerization-powered motor. *Angew. Chem. Int. Ed.* **50**, 9374–9377 (2011).
6. Orozco, J. *et al.* Artificial enzyme-powered microfish for water-quality testing. *ACS Nano* **7**, 818–824 (2013).
7. Gu, H., Chao, J., Xiao, S. J. & Seeman, N. C. A proximity-based programmable DNA nanoscale assembly line. *Nature* **465**, 202–205 (2010).
8. Lund, K. *et al.* Molecular robots guided by prescriptive landscapes. *Nature* **465**, 206–210 (2010).
9. Wickham, S. F. *et al.* Direct observation of stepwise movement of a synthetic molecular transporter. *Nature Nanotech.* **6**, 166–169 (2011).
10. Omabegho, T., Sha, R. & Seeman, N. C. A bipedal DNA Brownian motor with coordinated legs. *Science* **324**, 67–71 (2009).
11. Wickham, S. F. *et al.* A DNA-based molecular motor that can navigate a network of tracks. *Nature Nanotech.* **7**, 169–173 (2012).
12. Cha, T. G. *et al.* A synthetic DNA motor that transports nanoparticles along carbon nanotubes. *Nature Nanotech.* **9**, 39–43 (2014).
13. Yin, P., Choi, H. M. T., Calvert, C. R. & Pierce, N. A. Programming biomolecular self-assembly pathways. *Nature* **451**, 318–U314 (2008).
14. Bath, J., Green, S. J. & Turberfield, A. J. A free-running DNA motor powered by a nicking enzyme. *Angew. Chem. Int. Ed.* **44**, 4358–4361 (2005).
15. Pei, R. *et al.* Behavior of polycatalytic assemblies in a substrate-displaying matrix. *J. Am. Chem. Soc.* **128**, 12693–12699 (2006).
16. Perl, A. *et al.* Gradient-driven motion of multivalent ligand molecules along a surface functionalized with multiple receptors. *Nature Chem.* **3**, 317–322 (2011).
17. Fang, S., Lee, H. J., Wark, A. W., Kim, H. M. & Corn, R. M. Determination of ribonuclease H surface enzyme kinetics by surface plasmon resonance imaging and surface plasmon fluorescence spectroscopy. *Anal. Chem.* **77**, 6528–6534 (2005).
18. Yehl, K. *et al.* Catalytic deoxyribozyme-modified nanoparticles for RNAi-independent gene regulation. *ACS Nano* **6**, 9150–9157 (2012).
19. Liu, Y., Yehl, K., Narui, Y. & Salaita, K. Tension sensing nanoparticles for mechano-imaging at the living/nonliving interface. *J. Am. Chem. Soc.* **135**, 5320–5323 (2013).
20. Liu, Y. *et al.* Nanoparticle tension probes patterned at the nanoscale: impact of integrin clustering on force transmission. *Nano Lett.* **14**, 5539–5546 (2014).
21. Sbalzarini, I. F. & Koumoutsakos, P. Feature point tracking and trajectory analysis for video imaging in cell biology. *J. Struct. Biol.* **151**, 182–195 (2005).
22. Gal, N., Lechtman-Goldstein, D. & Weihs, D. Particle tracking in living cells: a review of the mean square displacement method and beyond. *Rheol. Acta* **52**, 425–443 (2013).
23. Domb, C., Gillis, J. & Wilmers, G. On shape and configuration of polymer molecules. *Proc. Phys. Soc.* **85**, 625 (1965).
24. Amit, D. J., Parisi, G. & Peliti, L. Asymptotic-behavior of the true self-avoiding walk. *Phys. Rev. B* **27**, 1635–1645 (1983).
25. Obukhov, S. P. & Peliti, L. Renormalization of the true self-avoiding walk. *J. Phys. A* **16**, L147–L151 (1983).
26. Family, F. & Daoud, M. Experimental realization of true self-avoiding walks. *Phys. Rev. B* **29**, 1506–1507 (1984).
27. Diehl, M. R., Zhang, K., Lee, H. J. & Tirrell, D. A. Engineering cooperativity in biomotor–protein assemblies. *Science* **311**, 1468–1471 (2006).
28. Østergaard, M. E. *et al.* Rational design of antisense oligonucleotides targeting single nucleotide polymorphisms for potent and allele selective suppression of mutant Huntingtin in the CNS. *Nucleic Acids Res.* **41**, 9634–9650 (2013).
29. Berna, J. *et al.* Macroscopic transport by synthetic molecular machines. *Nature Mater.* **4**, 704–710 (2005).
30. Eelkema, R. *et al.* Nanomotor rotates microscale objects. *Nature* **440**, 163–163 (2006).
31. Liu, Y. *et al.* Linear artificial molecular muscles. *J. Am. Chem. Soc.* **127**, 9745–9759 (2005).
32. Wang, W., Chiang, T. Y., Velegol, D. & Mallouk, T. E. Understanding the efficiency of autonomous nano- and microscale motors. *J. Am. Chem. Soc.* **135**, 10557–10565 (2013).

Author contributions

K.Y. conducted all the experiments and analysis, A.M. performed the simulations and theoretical validation, S.V. helped in the data analysis and validation of the theoretical model, Y.Z. helped with particle functionalization, Y.L. collected SIM data, M.F. assisted with SNP detection, K.S. and K.Y. wrote the manuscript with input from A.M. and E.R.W., K.S. oversaw all the aspects of the work and E.R.W. supervised and discussed the experiments with S.V.

Additional information

Supplementary information is available in the online version of the paper. Reprints and permissions information is available online at www.nature.com/reprints. Correspondence and requests for materials should be addressed to K.S.

Competing financial interests

The authors declare no competing financial interests.

Methods

Materials. All chemicals were purchased from Sigma-Aldrich unless otherwise stated. Stock solutions were made using Nanopure water (Barnstead Nanopure system, resistivity = 18.2 MΩ), herein referred to as DI water. Aminated silica beads (5 µm) were purchased from Bangs Laboratory (Product No. SA06N). The DNA fluorescence assay kit (Quant-iT OliGreen ssDNA kit) was acquired from Life Technologies (formerly Invitrogen) and was used to quantify DNA density on the particle surface. All oligonucleotides were custom synthesized by Integrated DNA Technologies and are summarized in Supplementary Table 1. RNase H was obtained from Takara Clontech (Product No. 2150A). Thin Au films were generated by using a home-built thermal evaporator system. All Au surface functionalization was carried out using IBIDI sticky-Slide VI$^{0.4}$ 17 × 3.8 × 0.4 mm channels.

Optical microscopy. BF and fluorescence images were acquired on a fully automated Nikon Eclipse Ti TIRF microscope controlled using the Elements software package (Nikon). Images were collected using the Evolve electron-multiplying charge-coupled device (EMCCD (Photometrics)) through a CFI Apo ×100 1.49 numerical aperture (NA) objective or a Plan Fluor ×20 0.50 NA objective. Fluorescence images of Cy3 were collected using an Intensilight Hg lamp epifluorescence source (Nikon) and a TRITC (tetramethylrhodamine isothiocyanate) filter cube set supplied by Chroma. An interferometric lock-in focus system (Perfect focus system) was used during the acquisition of time-lapse movies to minimize focus drift.

Super-resolution imaging of the fluorescence-depletion tracks. SIM images were acquired on a Nikon N-SIM system equipped with a CFI Apo ×100 1.49 NA objective and an Andor iXon EMCCD (60 nm per pixel). For each N-SIM image, nine images of a 3′-Cy3-RNA sample were acquired in different phases using a 561 nm laser as an excitation source and were reconstructed using the Nikon Element software package.

Thermal evaporation of gold films. A No. 1.5 glass slide (25 × 75 mm) was cleaned by sonication in DI water for five minutes. The sample was then subjected to a second sonication in fresh DI water for five minutes. Finally, the slide was sonicated in propanol for five minutes, and was subsequently dried under a stream of N$_2$. The cleaned slide was then introduced into a home-built thermal evaporator chamber and the pressure was reduced to $50 × 10^{-3}$ Torr. The chamber was purged with N$_2$ three times and the pressure was reduced to $1–2 × 10^{-7}$ Torr by using a turbo pump with a liquid N$_2$ trap. Once the desired pressure was achieved, a 1.5 nm film of Cr was deposited onto the slide at a rate of 0.2 Å s^{-1}, which was determined by a quartz-crystal microbalance. After the Cr adhesive layer had been deposited, 4 nm of Au was deposited at a rate of 0.4 Å s^{-1}. The Au-coated samples were used within one week of evaporation.

Fabrication of RNA monolayers. An IBIDI sticky-Slide VI$^{0.4}$ flow chamber was adhered to the Au-coated slide to produce six channels (17 × 3.8 × 0.4 mm dimensions). Prior to surface functionalization, each channel was washed with ~5 ml of DI water. Next, a densely packed DNA monolayer was assembled onto the Au surface by using published protocols in which 40 µl of a 1 µM 3′-disulfide-modified DNA strand (anchoring strand) was incubated with the surface for 12 hours under a buffer of high ionic strength (1 M KHPO$_4$)[33]. The chamber was then sealed by Parafilm to prevent evaporation. After incubation, excess DNA was removed from the channel using a ~5 ml DI water rinse. To block any bare gold sites and to maximize the hybridization of RNA to the DNA anchoring strand, the surface was backfilled with 100 µl of a 100 µM SH(CH$_2$)$_{11}$(OCH$_2$CH$_2$)$_6$OCH$_3$ (SH-PEG) solution in ethanol for six hours. Excess SH-PEG was removed by a ~5 ml rinse with ethanol and another ~5 ml rinse with water. Lastly, the RNA substrate was immobilized to the surface through hybridization of 100 µl of a complementary RNA/DNA chimera (100 nM) in 1 × PBS for 12 hours. The wells were sealed with Parafilm for each step to prevent evaporation and the resulting RNA monolayer remained stable for weeks, as determined by fluorescence imaging.

Determining RNA surface density. RNA surface density was determined by releasing the Cy3-tagged RNA from the surface by adding 100 µl of RNase A (100 µg ml^{-1} in 1 × PBS) and then quantifying the Cy3 fluorescence intensity in solution using a calibration curve obtained with the fluorescence microscope.

Microcontact printing of RNA tracks. To generate RNA tracks, SH-PEG barriers were initially patterned onto the thin gold film using established protocols[34]. Briefly, 30 µl of a 1 mM SH-PEG solution in ethanol was applied to a polydimethylsiloxane stamp with 3 µm wide parallel lines spaced at a 3 µm pitch. Next, the SH-PEG solution was dried under a stream of N$_2$ for one minute and the remaining solution was wicked away. The coated stamp was then brought into contact with the gold-film surface for 30 seconds. After contact, the stamp was peeled away from the substrate and used to print repeatedly without reapplying additional SH-PEG ink. After patterning the SH-PEG barriers onto the surface, the IBIDI sticky-Slide VI$^{0.4}$ flow chamber was adhered to the gold slide, and the substrate was prepared as described in the section 'Fabrication of RNA monolayers'. The RNA track-preparation protocol used an incubation with the DNA anchor solution of six hours rather than 12 hours.

Synthesis of azide-functionalized particles. First, azide-functionalized particles were synthesized by mixing 1 mg of 5 µm aminated silica beads (Bangs Laboratory) with 1 mg of N-hydroxysuccinimidyl azide heterobifunctional linker. This mixture was subsequently diluted in 100 µl of dimethylsulfoxide (DMSO) and 1 µl of a 10× diluted triethylamine stock solution in DMSO. The reaction proceeded overnight for 24 hours and the azide-modified particles were purified by adding 1 ml of DI water and centrifuging down the particles at 15,000 revolutions per minute (r.p.m.) for five minutes. The supernatant was discarded and the resulting particles were resuspended in 1 ml of DI water. This process was repeated seven times, and during the final centrifugation step the particles were resuspended in 100 µl of DI water to yield an azide-modified particle stock. The azide-modified particles were stored at 4 °C in the dark and were used within one month of preparation.

Synthesis of high-density DNA silica particles. High-density DNA-functionalized particles were synthesized by adding 5 nM (5 µl) of alkyne-modified DNA stock solution to 5 µl of azide-functionalized particles. The particles and DNA were diluted with 25 µl of DMSO and 5 µl of a 2 M triethyl ammonium acetate buffer (pH 7.0). Next, 4 µl from a 5 mM stock solution of ascorbic acid was added to the reaction as a reducing agent. Cycloaddition between the alkyne-modified DNA and azide-functionalized particles was initiated by adding 2 µl from a 10 mM Cu-TBTA (tris((1-benzyl-1H-1,2,3-triazol-4-yl)methyl)amine) stock solution in 55 vol% DMSO[35]. The reaction was incubated for 24 hours and the resulting DNA-functionalized particles were purified by centrifugation. Specifically, the particles were centrifuged at 15,000 r.p.m. for five minutes, after which the supernatant was discarded and the particles resuspended in 1 ml of a 1 × PBS and 10% Triton-X solution. This process was repeated seven times, with the particles resuspended in 1 ml 1 × PBS only for the fourth to sixth centrifugations. During the final centrifugation/wash, the particles were resuspended in 50 µl of 1 × PBS. The high-density DNA-functionalized particles were stored at 4 °C and protected from light.

Determining DNA particle surface density. The DNA surface density on the silica particles was determined by releasing the DNA using HF etching followed by quantifying the DNA concentration with a fluorescence assay. Initially, 50 µl of DNA-functionalized particles were diluted with 45 µl of PBS and 5 µl of concentrated (50% by vol.) HF. After 30 minutes of etching, DNA was assumed to be fully released from the surface based on a BF characterization of particle whittling (Supplementary Fig. 6). Subsequently, the DNA concentration was quantified using a commercial fluorescence assay to detect single-stranded DNA (Quant-iT OliGreen ssDNA kit, Invitrogen) following the published product protocol. The final DNA density was calculated by determining the concentration of particle stock using a haemocytometer.

Determination of RNase H surface kinetics. A monolayer of RNA/DNA duplexes was constructed by hybridizing a soluble complementary DNA strand to the RNA monolayer. Briefly, 100 µl of a DNA stock solution (100 µM) in 1 × PBS was added to the ssRNA surface. After one hour of hybridization, the excess DNA was washed away by rinsing the channel with 5 ml 1 × PBS, which was exchanged for 100 µl of RNase H reaction buffer (25 mM Tris pH 8.0, 8 mM NaCl, 37.5 mM KCl, 1.5 mM MgCl$_2$, 10 vol% formamide and 0.75% (g ml^{-1}) Triton X). The RNA hydrolysis reaction was initiated by the addition of 2 µl (five units) of RNase H from an enzyme stock of 7.2 µM (2.5 units µl^{-1}) enzyme, 500 µM DTT and 1 × PBS. The reaction progress was monitored by measuring the loss in surface RNA fluorescence over time. As the kinetic conditions satisfy the Michaelis–Menten requirements with a substrate RNA concentration at a ~60-fold excess over enzyme (1.2 nM), we determined k_{cat} by dividing the initial rate of reaction (V_{max}) by enzyme concentration ($V_{max} = k_{cat} × [enzyme]$)[36].

Particle translocation powered by RNase H. Initially, RNA-substrate surfaces were washed with 5 ml of PBS to remove excess unbound RNA. Next, DNA-functionalized particles were hybridized to the RNA substrate. Briefly, 5 µl of DNA-functionalized particles were diluted with 45 µl of PBS, which was added to the RNA substrate. Hybridization between the particles and the complementary RNA monolayer occurred over an incubation period of 30 minutes. After hybridization, particle translocation was initiated by buffer exchange with 100 µl of RNase H reaction buffer (25 mM Tris pH 8.0, 8 mM NaCl, 37.5 mM KCl, 1.5 mM MgCl$_2$, 10% formamide and 0.75% (g ml^{-1}) Triton X) and 2 µl (five units) of RNase H from an enzyme stock of 7.2 µM enzyme, 500 µM DTT and 1 × PBS. The microchannel was sealed with Parafilm to prevent evaporation. Particle tracking was achieved through BF imaging acquired at five second intervals using a MOSAIC ImageJ plugin[21]. High-resolution epifluorescence images (×100) of fluorescence-depletion tracks were acquired to verify that particle motion resulted from processive RNA hydrolysis. For high-resolution movies (×100), both BF and epifluorescence images were recorded at five second intervals. For control (blocked) particles, after DNA-particle hybridization with the surface, the remaining ssDNA on the particle was hybridized with a blocking strand (100 µM) in 1 × PBS for 30 minutes. Prior to buffer exchange, the particles were washed carefully with 2 ml PBS to remove excess DNA-blocking strand. For particle motion along the RNA-patterned tracks, a higher salt concentration of 150 mM KCl was used.

Smartphone-based SNP detection. Two focusing lenses (obtained from a toy laser pointer) were taped together and adhered to the cell-phone camera via double-sided tape. The smartphone was placed onto a lab jack, which was used to focus onto the sample. The sample was placed onto an optically transparent plastic sheet, with a battery-powered light-emitting diode positioned underneath for illumination. To minimize drift, tape was used to immobilize both the smartphone to the jack and the sample to the plastic sheet. Using the smartphone application Lapse It Pro, images were acquired at the desired time intervals, and the displacements were subsequently measured using ImageJ image-processing software. The reaction buffer required higher salt concentrations (110 mM KCl and 4.5 mM MgCl$_2$) because of the lower stability of the shorter sequences used in the SNP assay.

References

33. Peterson, A. W., Heaton, R. J. & Georgiadis, R. M. The effect of surface probe density on DNA hybridization. *Nucleic Acids Res.* **29,** 5163–5168 (2001).
34. Yan, L., Zhao, X. M. & Whitesides, G. M. Patterning a preformed, reactive SAM using microcontact printing. *J. Am. Chem. Soc.* **120,** 6179–6180 (1998).
35. Zhang, Y., Ge, C. H., Zhu, C. & Salaita, K. DNA-based digital tension probes reveal integrin forces during early cell adhesion. *Nature Commun.* **5,** 5167 (2014).
36. Johnson, K. A. & Goody, R. S. The original Michaelis constant: translation of the 1913 Michaelis–Menten paper. *Biochemistry* **50,** 8264–8269 (2011).